Research Square

Preprints are preliminary reports that have not undergone peer review.
They should not be considered conclusive, used to inform clinical practice,
or referenced by the media as validated information.

Illuminating early ZrC oxidation using ensemble small-cell DFT with dynamic gas management

Philip Würzner

pdwurzner@tudelft.nl

Delft University of Technology

Boyang Chen

Soochow University

Matthias Möller

Delft University of Technology

Sebastian Feld

Delft University of Technology

Qi-Jun Hong

Arizona State University

Yinglu Tang

Delft University of Technology

Article

Keywords: ZrC, ZrO2, ZrOx, Early Stage Oxidation, DFT, AIMD, Small-Cell

Posted Date: October 8th, 2026

DOI: https://doi.org/10.21203/rs.3.rs-11075897/v1

License: This work is licensed under a Creative Commons Attribution 4.0 International License.
Read Full License

Additional Declarations: No competing interests reported.

Illuminating early ZrC oxidation using ensemble small-cell DFT with dynamic gas management

Philip Würzner[1*], Boyang Chen[4,1], Matthias Möller[3], Sebastian Feld[3], Qi-Jun Hong[2*], Yinglu Tang[1*]

[1*]Faculty of Aerospace Engineering, Delft University of Technology, Delft, The Netherlands.
[2]School for Engineering of Matter, Transport and Energy, Arizona State University, Tempe, United States of America.
[3]Faculty of Electrical Engineering, Mathematics and Computer Science, Delft University of Technology, Delft, The Netherlands.
[4]School of Optoelectronic Science and Engineering, Soochow University, Suzhou, China.

*Corresponding author(s). E-mail(s): pdwurzner@tudelft.nl; qhong7@asu.edu; y.tang-5@tudelft.nl;
Contributing authors: boyangchen@suda.edu.cn; m.moller@tudelft.nl; s.feld@tudelft.nl;

Abstract

During zirconium carbide oxidation, liberated carbon can remain beneath the oxide or escape as gas, complicating the interpretation of mass measurements. We adapt the small-cell ensemble method using sixteen 140 ps *ab initio* molecular dynamics trajectories at 873–1273 K under a sustained high oxygen flux with gas removal. The average rates of net mass gain and total carbon transfer into gas or retained chains follow Arrhenius trends. Above 973 K, gas evolution levels off while total carbon transfer increases. The fraction of transferred carbon retained in chains rises from 40% at 973 K to 66% at 1273 K. Fits after 40 ps suggest declining carbon transfer rates over time, although not in every trajectory. These results show that carbon partitioning during early oxidation depends on temperature, with increasing temperature above 973 K favouring chain formation over gasification.

Keywords: ZrC, ZrO2, ZrOx, Early Stage Oxidation, DFT, AIMD, Small-Cell

1 Introduction

Zirconium carbide (ZrC) is an ultra-high-temperature ceramic (UHTC) considered for thermal protection systems in reusable launch vehicles and nuclear reactors for its ultra-high melting point (∼3800 K), high thermal conductivity, and high-temperature strength [1, 2]. However, poor oxidation resistance severely limits its use in oxygen-containing environments [2, 3] and an incomplete understanding of oxidation kinetics limits our ability to ameliorate this drawback. Reported rates and activation energies vary across studies, and although these inconsistencies have recently been unified into successive stages of a single temperature- and pressure-dependent process [4], the atomistic mechanisms driving each stage remain unclear, including how carbon retention and gasification affect the protectiveness of the growing oxide.

The oxidation of ZrC is modeled as proceeding through a zirconium oxycarbide (ZrC_xO_{1-x}) intermediate [3, 5–9]. The ZrC lattice can accommodate oxygen on up to ∼60% of its carbon-sublattice sites without a change in crystal structure, which may explain why this intermediate has proven difficult to observe directly [6–8, 10–12]. Oxygen substitutes the sublattice carbon, subsequently converting the oxycarbide to zirconium dioxide (ZrO_2), macroscopically described by [3, 8]:

$$\mathrm{ZrC} + \frac{1}{2}(1-x)\mathrm{O_2} \rightarrow \mathrm{ZrC}_x\mathrm{O}_{1-x} + (1-x)\mathrm{C} \tag{1}$$

$$\mathrm{ZrC}_x\mathrm{O}_{1-x} + \frac{1}{2}(1+3x)\mathrm{O_2} \rightarrow \mathrm{ZrO_2} + x\mathrm{CO_2}, \tag{2}$$

where x is the carbon retained in the oxycarbide and $(1-x)$ the carbon liberated.

A few nanometers of surface oxide form on ZrC in air already at room temperature [13]. At this temperature, Kato *et al.* identified a disordered, substoichiometric surface oxide following oxygen exposure of ZrC(100) [14]. Bulk conversion, however, begins only between ∼483 and ∼653 K across powder studies [6, 9, 15, 16]. Above these onsets, oxygen converts the zirconium into ZrO_2 while carbon is retained [8, 12, 15, 16], and CO_2 evolution follows only 120–210 K higher [9, 16]. At the ZrC/ZrO_2 interface, the retained carbon collects into an amorphous, carbon-rich layer with embedded ZrO_2 nanocrystals [3, 17, 18]. Although monoclinic ZrO_2 is the only stable phase below ∼1450 K at ambient pressure [19], the nanocrystals at the interface are metastable tetragonal and cubic forms, stabilized by their small size and oxygen deficiency [19], with the retained carbon stabilizing the cubic form [8, 12, 18]. They revert to monoclinic as they grow [3].

Lin et al. describe up to three successive stages during isothermal oxidation: a protective, diffusion-controlled parabolic stage (k_1), a partially protective stage (k_2), and reaction-controlled linear oxidation (k_3). They associate the loss of protectiveness with CO_2 evolution and scale cracking [4]. While the scale is intact, the dense inner oxide limits oxygen diffusion and carbon accumulates where the local oxygen supply is depleted [16, 18]. Once cracks pierce the oxide, the carbon-rich interfacial layer becomes the primary barrier [3]. Whether oxygen transport through this layer or reaction at the ZrC surface then sets the rate cannot be decided from the rate law alone, because both produce linear kinetics [20], and the two attributions indeed exist

in the literature [3, 4]. ^{18}O tracer measurements at 1073 K point to transport, but the extracted diffusivity is confounded [20] because oxygen simultaneously reacts within the layer to form ZrO_2 nanocrystals and CO/CO_2 [3].

Temperature and oxygen pressure govern how long each stage persists, or whether it occurs at all. At atmospheric pressure near and below 973 K, Lin et al. attribute the initial protective stage to carbon retention within a compact oxide scale [4]. At 1073 K, continuous thermogravimetry of spark-plasma-sintered samples resolves no fully protective stage [4], and quenched hot-pressed samples show a single linear regime from 15 minutes onward [3]. By 1273–1373 K, the interfacial carbon is itself gasified as CO_2, leaving a porous, detached monoclinic scale [3] that at 1273 K disintegrates to powder [21]. Oxygen pressure sets how much carbon is retained, with less remaining as pressure rises [7, 8] and interfacial carbon persisting to 1773 K at 20 Pa [17]. Across these studies, carbon retention is associated with compact scales and gasification with cracking and loss of protectiveness [3, 4]. The stages, however, are characterized only by macroscopic, mass-based kinetics whose activation energies span 70–292 $kJ\,mol^{-1}$ [6–9, 22] and depend on temperature, oxygen pressure, and sample preparation [4, 8], indicating that such measurements convolve the competing atomic-scale processes that they cannot individually resolve.

Prior density functional theory (DFT) works have characterized 0 K ZrC oxidation. Oxygen adsorbs dissociatively on ZrC surfaces [23] and binds strongly at carbon-adjacent sites across the group 4 carbides [24]. The C↔O surface exchange is exothermic, and carbon leaves as CO, not the CO_2 written in Eq. (2), only when a second oxygen adatom captures the displaced atom [25]. Dissolved oxygen occupies carbon vacancies in bulk ZrC_x [26]. Finally, ZrO_2 adheres strongly to the carbide through interfacial Zr–O bonds, with the strained oxide relaxing from its cubic to its tetragonal form at the interface [27, 28]. Dynamics entered this picture only recently. Kwon *et al.* showed by *ab initio* molecular dynamics (AIMD) that the adsorption, exchange, and substitution steps indeed play out in succession on the pristine (100) surface, with adsorbed oxygen extracting lattice carbon as CO within 130 fs and the vacancies left behind guiding subsequent oxygen substitution into the nascent oxycarbide [29], and Bai *et al.* observed the same rapid dissociative onset on a Zr-containing high-entropy carbide [30]. Both studies, however, span only 2–5 ps with a single fixed dose of oxygen, so the trajectories end where sustained oxide growth would begin, a restriction Bai *et al.* note explicitly. The competition between carbon retention and gasification thus remains unquantified.

Extending such trajectories within conventional DFT is expensive, and researchers often turn to reactive force fields (ReaxFF) [31, 32] or machine learning interatomic potentials (MLIPs) [33] to reach longer times and larger systems. These approaches, however, trade away quantum-mechanical accuracy or generalization to conditions outside their training data [34]. The timescale problem can instead be addressed within DFT itself. For equilibrium properties, the small-cell coexistence method of Hong and van de Walle showed that an ensemble of short simulations of 100–250-atom cells can replace a single prohibitively large calculation, with the statistics over independent runs providing both the observable and its uncertainty [35, 36].

We extend the small-cell framework from equilibrium phase coexistence to non-equilibrium surface oxidation. We implement a reactive gas-exchange protocol that sustains oxidation over AIMD timescales by replenishing O_2 and removing gaseous carbon molecules (Section 4.3). We run four independent cells at each of four temperatures spanning 873–1273 K for ∼140 ps, over an order of magnitude longer than previous oxidation AIMD, so that trajectory-to-trajectory spread provides the uncertainty on pathway-resolved oxidation kinetics. The trajectories quantify how carbon conversion and its partitioning between retained chains and gas depend on temperature during early oxide growth.

2 Results

The small-cell ensemble comprises 16 independent AIMD trajectories across four temperatures (873, 973, 1073, and 1273 K), each run for 140 ps under the reactive gas-exchange protocol of Section 4.3. The cell is initialized with 10 O_2 molecules in a gas phase twice the length of the bulk ZrC, which is itself initialized as a $3 \times 2 \times 2$ supercell. The time-averaged Hertz–Knudsen impingement fluxes for the four temperature ensembles differed by less than 15 % (Table 1), providing comparable mean external oxygen supplies. Variation between trajectories is used to assess sampling uncertainty.

Table 1 Simulation conditions aggregated over $N = 4$ trajectories per temperature, over 140 ps simulations (560 ps per temperature). Pressure and Flux time-averaged means ± standard deviation.

Temp (K)	**Pressure (bar)**	**Flux $\bar{J}$ ($10^{27}\,\mathbf{m^{-2}s^{-1}}$)**
873	59.9 ± 7.4	94.4 ± 11.6
973	61.7 ± 11.2	92.1 ± 16.8
1073	73.3 ± 8.7	104.3 ± 12.4
1273	78.2 ± 3.4	102.1 ± 4.5

2.1 A partially disordered oxide grows and carbon accumulates

At all temperatures an oxide forms and carbon accumulates at the ZrC/ZrO_2 interface (Fig. 1). Averaged over the last 10 % of the simulations (126–140 ps), the oxygen number density shows sharp periodic layering outward from the reaction front. For the 1073 and 1273 K surfaces, the detected oxygen layers approximately follow the carbide plane spacing and phase, while zirconium shows no comparable periodicity across the same region (Supplementary Section S1). This supports oxygen layering inherited from the carbide, although the density profiles alone do not establish the crystallinity of the oxide.

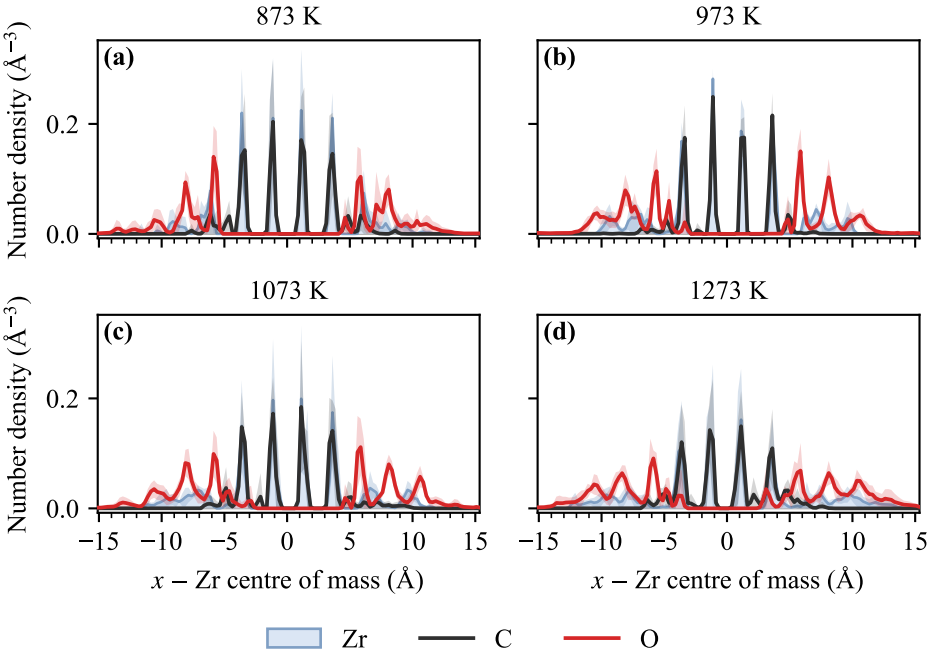


Fig. 1 Species number density profiles along the interface normal at each temperature, averaged over the final 10 % (126–140 ps) on a uniform 50 fs time grid. Grey shaded bands are ±1 s.d. across frames and the four independent trajectories.

2.2 Gasification is favoured at 973 K

The conversion of ZrC into ZrO_2 proceeds through several subreactions. When carbon is liberated from its lattice site by reaction (1) and by the conversion of the oxycarbide ZrC_xO_{1-x} into ZrO_2,

$$ZrC_xO_{1-x} + \frac{1+x}{2}O_2 \rightarrow ZrO_2 + xC, \tag{3}$$

the liberated carbon then resolves through one of two pathways. First of these pathways is gasification,

$$C + \frac{y}{2}O_2 \rightarrow CO_y, \tag{4}$$

where $y = 1$ or 2. The second pathway is retention by carbon coupling into chains,

$$C + C \rightarrow 2C_{\text{chain}}, \tag{5}$$

which enables a secondary channel for oxidation of carbon:

$$C_{\text{chain}} + \frac{y}{2}O_2 \rightarrow CO_y. \tag{6}$$

In our simulations, CO is the predominant gas product at each temperature (Table 2). The balance between pathways (4) and (5) may be quantified by the carbon retention ratio,

$$\phi_{\mathrm{C}} = \frac{n^{\mathrm{C}}_{\mathrm{chain}}}{n^{\mathrm{C}}_{\mathrm{chain}} + n^{\mathrm{C}}_{\mathrm{gas}}}, \tag{7}$$

where $n^{\mathrm{C}}_{\mathrm{chain}}$ is the number of carbon atoms currently in chains and $n^{\mathrm{C}}_{\mathrm{gas}}$ is the cumulative number removed as CO or CO_2. Similarly, the oxygen retention ratio,

$$\phi_{\mathrm{O}} = \frac{n^{\mathrm{O}}_{\mathrm{scale}}}{n^{\mathrm{O}}_{\mathrm{scale}} + n^{\mathrm{O}}_{\mathrm{gas}}}, \tag{8}$$

where $n^{\mathrm{O}}_{\mathrm{scale}}$ is the number of oxygen atoms in the oxide scale and $n^{\mathrm{O}}_{\mathrm{gas}}$ is the cumulative number of oxygen atoms removed in CO or CO_2.

Table 2 Kinetic product details at 140 ps. Product counts are summed over the four trajectories per temperature. Chain length is the number of carbon atoms connected by C–C bonds within the confirmed chain population; the mean and maximum are taken over all such chains pooled across the four trajectories. ϕ_{C} and ϕ_{O} are the observed retention fractions (Eqs. 7–8).

	Reaction products				$\mathrm{C_{chain}}$ **Length**		**Ratios**		
Temp. (K)	$n^{\mathrm{CO}}_{\mathrm{gas}}$	$n^{\mathrm{CO_2}}_{\mathrm{gas}}$	$n^{\mathrm{O}}_{\mathrm{scale}}$	$n^{\mathrm{C}}_{\mathrm{chain}}$	**Avg.**	**Max**	$\mathrm{CO/CO_2}$	ϕ_{C}	ϕ_{O}
873	21	10	131	35	2.69	4	2.1	0.53	0.76
973	43	4	163	31	2.82	4	10.8	0.40	0.76
1073	36	2	170	48	3.00	6	18.0	0.56	0.81
1273	33	3	208	69	3.29	8	11.0	0.66	0.84

Table 2 summarizes the product partitioning at 140 ps. At 873 K the carbon pathways are balanced, $\phi_{\mathrm{C}} = 0.53$ and the formation of CO_2 is higher than at the other temperatures. Among the temperatures studied, only the 973 K ensemble has more gasified than retained carbon, $\phi_{\mathrm{C}} = 0.40$. At higher temperatures the balance shifts towards retention, with ϕ_{C} rising to 0.56 at 1073 K and 0.66 at 1273 K, accompanied by longer chains. Oxygen partitioning varies less with temperature. ϕ_{O} increases from 0.76 to 0.84, so roughly 80 % of the reacted oxygen resides in the scale at every temperature, with retention highest where the oxide grows fastest. The ratios calculated in Table 2 are simulation time-dependent. Over 40–140 ps, $\phi_{\mathrm{O}}(t)$ varies less than $\phi_{\mathrm{C}}(t)$, which generally shifts toward greater retention (Supplementary Section S2). Because chain carbon can still gasify (Eq. 6), retention is defined as chain occupation at 140 ps rather than as chain entry. To check for gasification after chain formation, we identified gasified carbons that had previously formed C–C bonds lasting at least 0.2 ps. Of the 152 carbons gasified by 140 ps, 8 had previously entered a chain, while 183 carbons were in chains at 140 ps.

To assess uncertainty from the four-trajectory ensembles, we generated 10,000 synthetic ensembles per temperature by redrawing the four trajectories with replacement

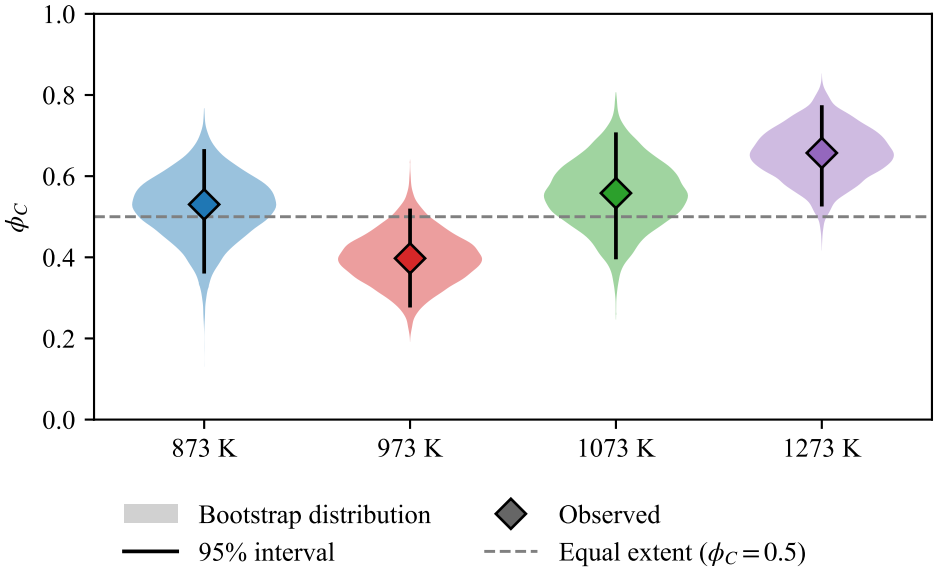


Fig. 2 Bootstrap distributions of ϕ_C (Eq. 7) at 140 ps. Violins show 10 000 trajectory resamples per temperature (with replacement, then outcomes resampled within each). Black bars show the 95 % confidence interval.

and resampling the carbon products within each draw according to their carbon product distribution (Fig. 2, Section 4.4). ϕ_C falls below 0.5 in 94 % of these ensembles at 973 K, versus 34 %, 23 %, and 1 % at 873, 1073, and 1273 K. The minimum in ϕ_C at 973 K appears in 85 % of resamples. These results support a preference for gasification at 973 K, although its 95 % interval crosses $\phi_C = 0.5$. The ordering of 1073 and 1273 K is also unresolved (Supplementary Section S2).

2.3 Total carbon commitment follows an Arrhenius trend

At 140 ps roughly half of the lattice carbon remains unreacted, and the pool of unreacted carbon depletes as it converts. A rate counted over atoms and elapsed time keeps reacted carbons in its denominator after they are gone, understating the rate more where conversion runs further, which would tilt the fitted Arrhenius slope (Supplementary Section S3). A survival framework removes this bias by assigning each of the 192 lattice carbons per temperature its time at risk, the event time for carbon that reacts and the full window for carbon that does not. Once liberated (Equation 3), a carbon commits to one of two competing states, gas when it desorbs as CO or CO_2, and chain when it enters the chain state it still occupies at 140 ps. The event counts are identical by construction to the gas and chain columns of Table 2, so the rates that follow are the kinetics behind the partitioning of Section 2.2.

We summarize commitment over the full 140 ps using a constant-rate model, whose maximum-likelihood estimate is

$$\lambda = \frac{n_{\mathrm{ev}}}{\sum_i t_i}, \tag{9}$$

where n_{ev} counts the commitments to a state and t_i is the observation time of carbon i (time to commit to a gas or chain state or 140 ps if uncommitted). Because the two commitments drain the same pool of uncommitted carbon, the gas and chain rates share one exposure and sum to the total commitment rate. Each estimate carries an approximate model-based 95 % interval (Supplementary Table S3, Section 4.5).

The estimated total commitment rate, used here as a proxy for liberation, rises from 3.0×10^{-3} to 5.8×10^{-3} ps^{-1} between 873 and 1273 K and follows an Arrhenius trend with an apparent activation energy of 0.15 ± 0.06 eV (15 ± 6 kJ mol^{-1}) ($R^2 = 0.99$, Fig. 3a). The uncertainty is the trajectory-stratified bootstrap standard deviation of the fitted slope (Supplementary Section S3).

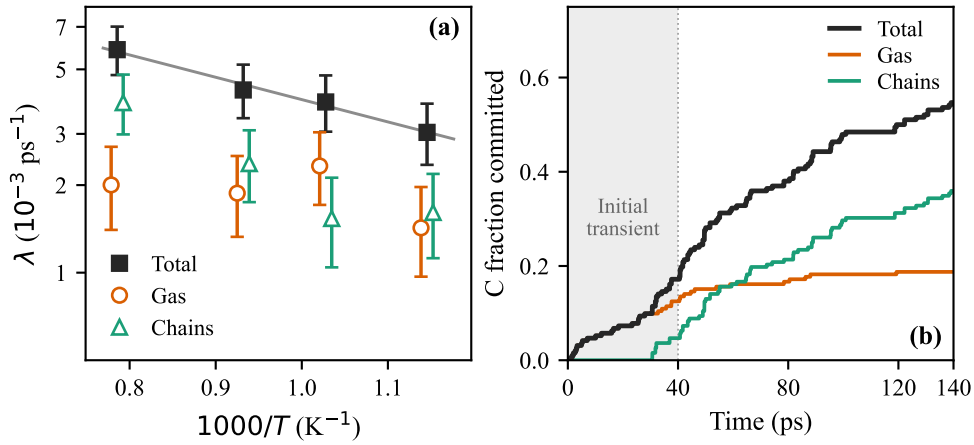


Fig. 3 Competing kinetics of carbon commitment. (a) Total committed rate λ (squares), estimated from all commitment times and times at risk across the full 140 ps window (Section 4.5), with its Arrhenius fit (0.15 eV, solid line), and its gas (circles) and chain (triangles) channels, which sum to it exactly. Error bars are approximate model-based 95 % intervals of the constant-rate estimates (Eq. 9). (b) Cumulative fractions of lattice carbon committed to gas, chains and their total at 1273 K. Shading marks the first 40 ps.

The gas commitment rate rises from 1.4×10^{-3} to 2.3×10^{-3} ps^{-1} between 873 and 973 K and levels off above 973 K (1.9×10^{-3} and 2.0×10^{-3} ps^{-1} at 1073 and 1273 K). The chain rate increases from 1.6×10^{-3} to 3.8×10^{-3} ps^{-1} over 873–1273 K. Above 973 K, the additional carbon conversion therefore primarily contributes to retained chains.

We tested whether the rates change over time, since the whole-run estimates average over the development of the oxide and carbon-rich interface. At 1273 K, cumulative commitment grows slowly at first, followed by a faster rise and then more gradual growth (Fig. 3b). We therefore fitted a Weibull model over 40–140 ps to reduce the

influence of the initial transient. Its shape parameter ρ describes how the commitment rate per remaining uncommitted atom changes over time: $\rho < 1$ a declining rate, and $\rho > 1$ an increasing rate. Fits to the combined trajectories give total shapes below one at all four temperatures ($\rho = 0.72$–0.85), suggesting declining commitment rates during this interval. This trend is not shared by every individual trajectory (Supplementary Section S3). For gas commitment, the fitted shapes range from $\rho = 0.51$ to 0.63 at 973–1273 K, compared with 0.99 at 873 K. Chain commitment gives shapes between 0.78 and 1.03 across all four temperatures. At 973–1273 K, the fits therefore suggest a steeper decline in gas commitment than in chain commitment, consistent with an increasing contribution of chains to later events.

2.4 Net mass gain and carbon partitioning

The net mass of the solid combines oxygen uptake and carbon loss as gas. Each oxygen retained in the scale adds 16.0 amu, while each carbon lost as gas removes 12.0 amu. The resulting signal rises smoothly at every temperature (Fig. 4a), and its average rates over 20–140 ps fit a single Arrhenius line with an apparent activation energy of 0.22 ± 0.04 eV (21 ± 3 kJ mol^{-1}, trajectory-stratified bootstrap standard deviation, Supplementary Section S3) at $R^2 = 0.999$ (Fig. 4b). Oxygen uptake increases with temperature and dominates the mass gain, while carbon loss to gas is smaller and peaks at 973 K. More carbon enters chains than gas at three of the four temperatures (Section 2.2), but chain formation does not change the mass of the solid.

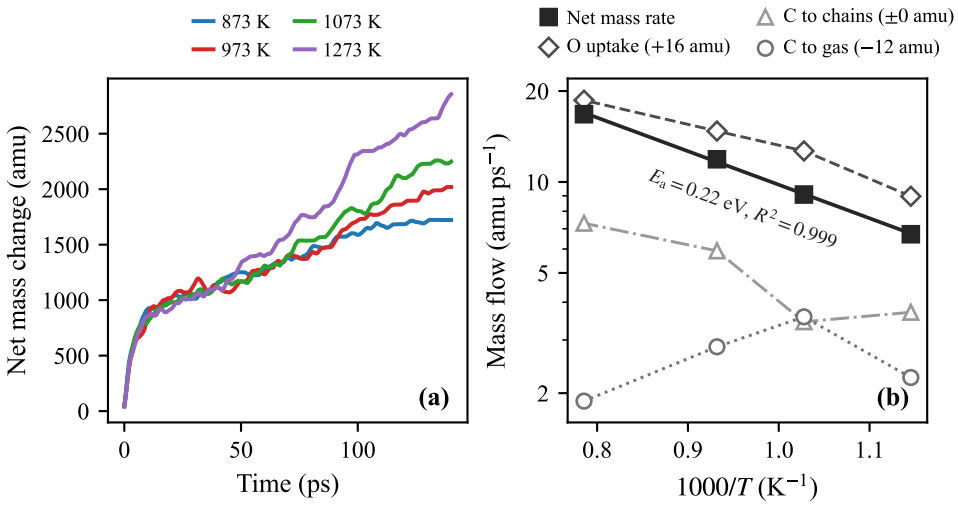


Fig. 4 Net mass gain and component flows. (a) Net mass change of the solid, summed over the four cells per temperature. (b) The mass flows behind the net rate over 20–140 ps (Section 4.6). The net rate follows a single Arrhenius line (0.22 ± 0.04 eV, $R^2 = 0.999$).

3 Discussion

In our ZrC oxidation simulations, the total carbon commitment rate, averaged over the full 140 ps, increases with temperature. Above 973 K, gas evolution levels off while chain formation increases, shifting the product balance towards retention (Sections 2.3 and 2.2). Faster release of lattice carbon therefore does not necessarily lead to faster carbon gas formation. Bartlett similarly described zirconium oxidation as liberating carbon that subsequently burns at its own rate [7]. Oxygen replenishment and gas removal allow us to follow this competition beyond the initial surface reactions accessible in earlier short AIMD studies [29, 30], into a regime where gasification and carbon aggregation proceed together.

The post-40 ps fits suggest declining total commitment rates at all four temperatures, although this trend is not shared by every trajectory (Supplementary Section S3). Chain commitment typically begins after a delay; at 973–1273 K, the gas rate declines more steeply than the chain rate. As the Zr–O network grows, it could restrict oxygen access to displaced carbon or impede its escape, while nearby carbon atoms provide opportunities for C–C bonding. Restricted oxygen access would be consistent with Shimada's attribution of interfacial carbon deposition to low local oxygen activity beneath the oxide [16]. Such retention during oxide growth is also observed in ReaxFF simulations of SiC oxidation, where carbon accumulates alongside the oxide before reacting with oxygen within it [31]. Preferential consumption of the most accessible lattice carbon could contribute to the declining commitment rate. The fits do not separate this effect from changes in oxygen access, carbon transport or aggregation.

Surface spectroscopy identifies substoichiometric ZrO_x during initial oxygen exposure, with Kato reporting a disordered surface layer after oxygen dosing at room temperature [14, 25]. Kato also inferred substrate-related lateral periodicity after annealing the oxygen-dosed surface to 1273 K, which reduced the oxide towards an ordered ZrO-like state [14]. In our simulations, oxygen layering develops normal to the interface during continued oxidation and retains the carbide plane spacing (Fig. 1), suggesting that the substrate influences the structure of the nascent oxide. Beneath the experimental oxide, microscopy and Raman spectroscopy show amorphous carbon with embedded zirconia nanocrystals [3, 17, 18]. The interfacial chains in our simulations may be a precursor to this carbon-rich layer.

Given that oxygen uptake adds mass, gasification removes carbon, and chain formation leaves the mass unchanged, net mass gain alone cannot determine carbon partitioning. Thermogravimetric studies inferred retained carbon from mass gain exceeding that expected for complete conversion to ZrO_2 [7, 16]. During partial conversion, however, different combinations of oxygen uptake and carbon loss can produce the same net mass. Despite the changing product balance, the average net mass rate follows an Arrhenius relation with an apparent activation energy of 0.22 ± 0.04 eV (Fig. 4), compared with 0.15 ± 0.06 eV for the average total carbon commitment rate (Section 2.3). Their activation energies cannot be distinguished within the present uncertainty (Supplementary Section S3). Additionally, neither fit identifies the barrier of a specific atomic reaction step. Lin *et al.* report apparent activation energies of

14–38 kJ mol^{-1} for their linear oxidation stage over 1073–1273 K as the oxygen concentration varies from 2 to 21 % [4]. Our net-mass value of approximately 21 kJ mol^{-1} falls within this range, but this does not show that the same process controls oxidation.

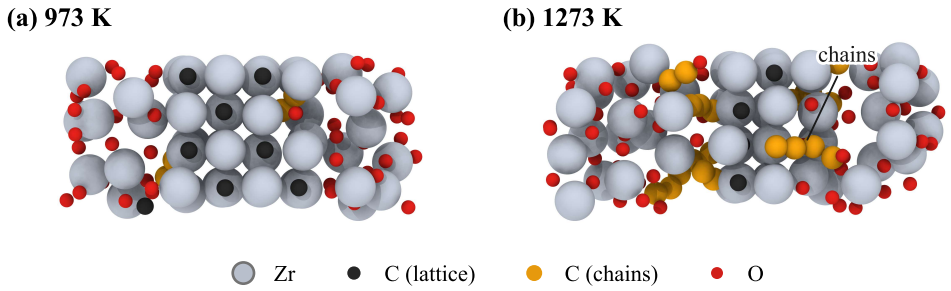


Fig. 5 Illustrative final configurations at 140 ps. Zirconium is grey, lattice carbon black, chain carbon amber, and oxygen red. (a) The 973 K cell with chain count nearest the four-cell median. (b) The 1273 K cell with the largest chain reservoir. Carbon chains occupy the gap between the carbide and the displaced oxide.

In our simulations, carbon accumulates while the post-40 ps fits suggest declining commitment rates. The fits do not establish whether retained carbon contributes to this slowdown. Barnier and Thevenot report substantial carbon retention in zirconium oxycarbides despite slightly lower oxidation resistance than zirconium carbide [9]. For a more developed layer, however, Gasparrini *et al.* attribute the oxidation rate at 1073 K to oxygen diffusion through the carbon–zirconia intermediate layer [3]. These observations suggest that carbon retention must be considered alongside the structure and transport properties of the surrounding layer. The chains in our final structures occupy the gap between the carbide and displaced oxide (Fig. 5), raising a further question about their effect on scale adhesion. Lin *et al.* associate CO_2 formation with cracking and loss of scale protectiveness [4], whilst Bellucci *et al.* attribute gas evolution during cooling to cracks exposing retained carbon to oxygen [12]. Carbon gasification and scale damage may thus reinforce one another, with their sequence depending on the thermal and exposure history.

Our trajectories distinguish carbon in chains from carbon still in the carbide lattice. Experiments likewise need to identify the form of retained carbon as well as its amount. Bellucci *et al.* and Lin *et al.* combined gas analysis with spectroscopic and microscopic characterization [4, 12]. Extending this approach with conversion-depth measurements in comparable regions would relate carbon accumulation to carbide consumption, while recording crack formation would help establish the sequence of carbon loss and scale damage. To test carbon's effect directly, simulations could vary interfacial carbon content while keeping temperature, oxygen supply, the extent of carbide conversion, and oxide thickness and structure comparable. Tracking oxygen arrival and carbon liberation at the carbide would then test whether retained carbon limits oxygen access and slows conversion, while adhesion calculations would examine how it changes the energy needed to separate oxide from carbide.

Four independent trajectories at each temperature sample different reaction pathways under the gas-exchange protocol (Section 4.3). The small-cell ensemble approach [35] uses this variation to estimate sampling uncertainty, although replication does not establish convergence with cell size. The small slab and short trajectories restrict the study to early growth; mature scale development and fracture require larger cells and longer observation times. The imposed oxygen flux and prompt removal of gaseous products constrain the rates and product balance to the modelled exposure conditions. The calculations use a stoichiometric (100) surface and non-spin-polarized DFT; initial carbon vacancies, other facets, and triplet gas-phase oxygen are outside this comparison. Under these conditions, the average rate of carbon conversion follows an Arrhenius trend, but its partitioning between gas and retained chains changes with temperature. Above 973 K, faster conversion increasingly produces retained carbon rather than additional gas.

4 Methods

4.1 DFT and AIMD setup

All calculations were performed using density functional theory (DFT) as implemented in the Vienna Ab initio Simulation Package (VASP) [37]. The projector-augmented wave (PAW) method was used to describe electron-ion interactions, and the Perdew-Burke-Ernzerhof (PBE) generalized gradient approximation (GGA) [38] was employed for the exchange-correlation functional.

The Brillouin zone was sampled using a single special k-point at $(0.25, 0.25, 0.25)$ [39]. The plane-wave energy cutoff was set to 400 eV. The electronic self-consistency loop was set to converge to a tolerance of 10^{-4} eV. Electronic occupancies were determined using Fermi-Dirac smearing, with the smearing width set to the thermal energy ($k_B T$) corresponding to each target simulation temperature (873–1273 K). Standard pseudopotentials were used for O ($2s^2 2p^4$) and C ($2s^2 2p^2$), while a semi-core potential was employed for Zr, treating 12 electrons as valence with a frozen [Ar]$3d^{10}$ core ($4s^2 4p^6 5s^2 4d^2$).

Non-spin-polarized DFT was used throughout, so the triplet ground state of gas-phase O_2 is not represented. The effect of this approximation on relative pathway rates has not been tested.

To model the oxidation process, a simulation cell was constructed consisting of a solid ZrC slab and a gaseous O_2 phase. A $3 \times 2 \times 2$ supercell of bulk ZrC (comprising 48 Zr and 48 C atoms) was cleaved along the (100) surface to create a $\sim$ 14.1 Å thick slab. A vacuum region twice the thickness of the slab was added to separate the periodic images, creating two exposed pristine surfaces. All atoms within the slab were allowed to move dynamically without any constrained bulk layers. This vacuum was subsequently filled with 10 O_2 molecules (20 O atoms) aligned along the x-axis. Their initial locations were determined via a differential evolution optimization algorithm to maximize the minimum distance from any molecule to any other atom in the cell.

All AIMD trajectories were propagated in the NVT ensemble using a Nosé-Hoover thermostat to maintain the target temperatures of 873 K, 973 K, 1073 K, and 1273 K. While the continuous MD integration formally conserves the number of particles (N),

our framework periodically handled the discrete addition of O_2 and removal of carbon gases, effectively modeling an open, reactive system. The molecular dynamics time-step size was dynamically adjusted within a range of 0.8 to 1.6 fs by SLUSCHI [35]. For each temperature, 4 independent small cells were simulated for 140 ps.

4.2 Bond detection

Atomic connectivity was determined using pair-specific distance cutoffs for gas species identification (O_2, CO, CO_2) and coordination analysis. A pair was classified as bonded when its Cartesian separation, evaluated using the minimum-image convention for periodic boundary conditions [40], satisfied

$$r_{ij} < r_{ij}^{\mathrm{cut}}, \tag{10}$$

where r_{ij}^{cut} is the cutoff for the species pair. The cutoffs were 2.31 Å for C–C, 2.15 Å for C–O, 3.33 Å for Zr–C, 3.17 Å for Zr–O, and 1.98 Å for O–O. Each oxygen atom was restricted to a maximum of one O–O bond, assigned by shortest pairwise distance.

4.3 Dynamic gas exchange protocol

Extending the equilibrium small-cell framework [35, 36] to oxidation requires three modifications. The system becomes open, with oxygen continuously supplied and gaseous products removed to prevent artificial back-pressure. The run tracks a sustained, irreversible transformation rather than an equilibrium endpoint, and the targets are mechanistic observables, oxide structure, product distribution, and rates, averaged over the trajectory ensemble.

To sustain the oxygen supply, the reactive gas-exchange protocol replenishes the O_2 population using a threshold that tracks the available gas volume. We estimate the resulting impingement flux using the Hertz–Knudsen expression

$$J = \frac{N}{V_{\mathrm{gas}}}\sqrt{\frac{k_B T}{2\pi m}}, \tag{11}$$

where N is the free O_2 molecule count, V_{gas} the available gas volume, m the O_2 molecular mass, and k_B the Boltzmann constant. The equivalent pressure form $J = P/\sqrt{2\pi m k_B T}$ relates the estimated flux to the O_2 partial pressures quoted alongside it. The gas volume is re-evaluated as the oxide grows, the instantaneous O_2 count is smoothed to filter transient adsorption and desorption, and a molecule is added whenever the smoothed count falls below a threshold that tracks the shrinking gas volume, so the addition rate follows the receding gas phase rather than a fixed molecule count. Newly added molecules are placed to maximize their distance from existing atoms. The threshold definitions and implementation parameters are given in Supplementary Section S4. A related stepwise O_2 dosing scheme has been used to model the thermal oxidation of Si(100) [41]. Carbide oxidation additionally requires the removal of volatile carbon oxides, which silicon oxidation does not produce.

Carbon-containing gas products (CO and CO_2) are permanently removed from the simulation cell upon detection. A molecule is classified as a detached gas product if the bond criteria (Section 4.2) identify it as an isolated two- or three-atom molecule that is not O_2. Single unbound atoms are excluded from removal and retained within the cell.

The time-averaged impingement flux, averaged over the four trajectories at each temperature, ranged from 0.92 to 1.04×10^{29} m^{-2} s^{-1}; individual trajectory averages ranged from 0.81 to 1.18×10^{29} m^{-2} s^{-1} (Supplementary Table S4). Rates are reported without flux normalization. As a sensitivity check, dividing the rates by the corresponding mean flux changed the apparent activation energies from 0.22 to 0.20 eV for net mass gain and from 0.15 to 0.13 eV for total carbon commitment, within their respective bootstrap uncertainties (Supplementary Section S4).

4.4 Bootstrap intervals for carbon partitioning

The confidence intervals and ordering probabilities of Section 2.2 come from a two-level bootstrap that mirrors the data hierarchy. At the outer level the four trajectories per temperature are drawn with replacement, and at the inner level the carbon outcomes of each drawn trajectory are resampled with replacement from that trajectory's own outcomes, with the atom as the resampling unit. Intervals are the 2.5th and 97.5th percentiles of 10 000 resampled ϕ_C values, and every dominance or ordering statement quotes the fraction of resamples in which it holds, a resampled probability rather than a p-value. The scheme is seeded at 20260715, and the design rationale is given in Supplementary Section S2.

4.5 Competing-risks survival analysis of carbon commitment

We estimated the rates in Section 2.3 using competing-risks survival analysis with cause-specific hazards. All 192 lattice carbons per temperature contribute their observed time before commitment, including those that remain uncommitted (Supplementary Section S3). Gas commitment occurs at the audited desorption time (Supplementary Section S6). Chain commitment occurs when a carbon enters the confirmed chain state that it still occupies at 140 ps, using the classification in Supplementary Section S7. The event counts match the gas and chain columns of Table 2.

Carbon uncommitted at 140 ps is censored at that time. The five atoms removed by the bookkeeping artifact are censored at their deletion times (Supplementary Section S6). Sensitivity to the release-time definition and treatment of displaced but uncommitted carbon is examined in Supplementary Section S3.

Because gas and chain commitments drain the same pool of lattice carbon, the two cause-specific rates share one exposure and sum exactly to the total commitment rate. Each constant-rate estimate (Equation 9) carries an approximate model-based 95 % interval $\left[\chi^2_{0.025}(2d)/2T_{\mathrm{exp}},\ \chi^2_{0.975}(2d)/2T_{\mathrm{exp}}\right]$, where d counts the commitments and T_{exp} is the summed time at risk. These intervals assume a constant rate and independent carbon records; trajectory-level variation is assessed separately by bootstrap (Supplementary Section S3). The committed fractions of Fig. 3b are cumulative incidence functions.

Time stationarity of each rate is tested using a Weibull hazard with shape ρ, fitted with lifelines 0.30.0 [42]. To reduce the influence of the initial transient visible in Fig. 3b, we fit the interval from 40 to 140 ps. Only carbon still uncommitted and under observation at 40 ps is included, with 40 ps subtracted from subsequent event and censoring times. The constant-rate model is recovered at $\rho = 1$; shapes below or above one indicate declining or increasing rates per remaining uncommitted atom, respectively. The rate estimates and Arrhenius analysis in Fig. 3a use the full 140 ps window. The likelihood-ratio statistic $2\,\Delta \log L$ is compared against a χ^2 distribution with one degree of freedom.

All estimates are deterministic given the event ledger, and the bootstrap probabilities of Supplementary Section S3 use seed 20260715.

4.6 Reconstruction of net mass gain

We calculated net mass change from oxygen retained in the scale and carbon lost as gas (Fig. 4). Each oxygen bound into the scale adds 15.999 amu and each carbon lost as gas removes 12.011 amu, values the text rounds to 16.0 and 12.0. An oxygen counts as bound into the scale when it belongs to a bonded component of the network of Section 4.2 that contains at least one zirconium, after intact O_2 molecules, identified by shortest-first unique O–O pairing below 1.98 Å, are excluded. Because the trajectories carry different time stamps, each is interpolated onto a common 0.1 ps grid before the four cells are summed, and the summed series is smoothed with a 2 ps moving average to remove the flicker of transiently bonded atoms. Flow slopes are fitted on 20 to 140 ps, excluding the initial dose burst, and the Arrhenius fit acts on the four net rates. The reconstruction is deterministic and involves no resampling.

Data availability

Product counts for the individual trajectories are provided in the supplementary information. The simulation inputs are available from the corresponding author upon reasonable request.

Code availability

The oxidation framework is available at https://github.com/Philipwur/SGUSCHI. At the time of submission, the code supports VASP-based workflows for basic cubic structures. The analysis scripts are available from the corresponding author upon reasonable request.

Acknowledgments

We would like to thank the HPC team at the DelftBlue supercomputer for their support.

Funding

This work was funded by QAIMS Lab support and the Delft AI Initiative, with contribution from the Faculty of Aerospace Engineering.

Author contributions

PW, QJH, and YT designed the research and interpreted results; PW programmed the framework for the simulations and analyses with support from QJH; BC, MM, and SF contributed to methodological and writing review; PW wrote the manuscript with input from all authors.

Competing Interests

The authors declare no competing interests.

References

[1] Sengupta, P., Manna, I.: Advanced high-temperature structural materials for aerospace and power sectors: A critical review. Transactions of the Indian Institute of Metals **72**(8), 2043–2059 (2019) https://doi.org/10.1007/s12666-019-01598-z

[2] Peterson, G.R., Carr, R.E., Marinero, E.E.: Zirconium carbide for hypersonic applications, opportunities and challenges. Materials **16**(18) (2023) https://doi.org/10.3390/ma16186158

[3] Gasparrini, C., Chater, R.J., Horlait, D., Vandeperre, L., Lee, W.E.: Zirconium carbide oxidation: Kinetics and oxygen diffusion through the intermediate layer. Journal of the American Ceramic Society **101**(6), 2638–2652 (2018) https://doi.org/10.1111/jace.15479

[4] Lin, Y.-C., Brouwer, H., Popovich, V., Tang, Y.: Three-stage oxidation kinetics and passivation mechanism of spark plasma sintered ZrC ultra-high temperature ceramic. Journal of the European Ceramic Society **46**(2), 117757 (2026) https://doi.org/10.1016/j.jeurceramsoc.2025.117757

[5] Voitovich, R., Pugach, E.A.: High-temperature oxidation of ZrC and HfC. Soviet Powder Metallurgy and Metal Ceramics **12**(11), 916–921 (1974)

[6] Shimada, S., Ishii, T.: Oxidation kinetics of zirconium carbide at relatively low temperatures. Journal of the American Ceramic Society **73**(10), 2804–2808 (1990) https://doi.org/10.1111/j.1151-2916.1990.tb06678.x

[7] Bartlett, R.W., Wadsworth, M.E., Cutler, I.B.: The oxidation kinetics of zirconium carbide. Trans. AIME **Vol: 227** (1963) https://www.osti.gov/biblio/4724730

[8] Rama Rao, G.A., Venugopal, V.: Kinetics and mechanism of the oxidation of ZrC. Journal of Alloys and Compounds **206**(2), 237–242 (1994) https://doi.org/10.1016/0925-8388(94)90042-6

[9] Barnier, P., Thevenot, F.: A comparative study of the oxidation resistance of zirconium carbide and zirconium oxycarbide. European Journal of Solid State and Inorganic Chemistry **25**(5-6), 495–508 (1988) https://doi.org/10.1002/chin.198937031

[10] Kucheryavaya, A., Lenčéš, Z., Šajgalík, P., Harmuth, H.: Zirconium oxycarbides and oxycarbonitrides: A review. International Journal of Applied Ceramic Technology **20**(2), 541–562 (2023) https://doi.org/10.1111/ijac.14188

[11] Sakar, S.K., Miller, A.D., Mueller, J.I.: Solubility of oxygen in ZrC. Journal of the American Ceramic Society **55**(12), 628–630 (1972) https://doi.org/10.1111/j.1151-2916.1972.tb13457.x

[12] Bellucci, A., Gozzi, D., Kimura, T., Noda, T., Otani, S.: Zirconia growth on zirconium carbide single crystals by oxidation. Surface and Coatings Technology **197**(2), 294–302 (2005) https://doi.org/10.1016/j.surfcoat.2004.05.035

[13] Fang, D., Wang, C., Lv, C., Lv, Y., Huang, G., Yang, J., Pan, S.: XPS studies of surface oxidation of metal carbides. Fullerenes, Nanotubes and Carbon Nanostructures **30**(7), 718–726 (2022) https://doi.org/10.1080/1536383X.2021.2014456

[14] Kato, S., Ozawa, K.-i., Edamoto, K., Otani, S.: Photoelectron spectroscopy study of the oxidation of ZrC(100). Japanese Journal of Applied Physics **39**(9R), 5217 (2000) https://doi.org/10.1143/JJAP.39.5217

[15] Cheng, C., Xie, W., Li, H., Fu, Q.: Oxygen adsorption on ideal ZrB_2 and ZrC surfaces. Journal of Alloys and Compounds **830**, 154655 (2020) https://doi.org/10.1016/j.jallcom.2020.154655

[16] Shimada, S.: A thermoanalytical study on the oxidation of ZrC and HfC powders with formation of carbon. Solid State Ionics **149**(3), 319–326 (2002) https://doi.org/10.1016/S0167-2738(02)00180-7

[17] Shimada, S., Yoshimatsu, M., Inagaki, M., Otani, S.: Formation and characterization of carbon at the ZrC/ZrO_2 interface by oxidation of ZrC single crystals. Carbon **36**(7), 1125–1131 (1998) https://doi.org/10.1016/S0008-6223(98)00087-6

[18] Shimada, S., Inagaki, M., Suzuki, M.: Microstructural observation of the ZrC/ZrO_2 interface formed by oxidation of ZrC. Journal of Materials Research **11**(10), 2594–2597 (1996) https://doi.org/10.1557/JMR.1996.0326

[19] Shukla, S., Seal, S.: Mechanisms of room temperature metastable tetragonal phase stabilisation in zirconia. International Materials Reviews **50**(1), 45–64 (2005) https://doi.org/10.1179/174328005X14267

[20] Crank, J.: Simultaneous diffusion and chemical reaction. The Mathematics of Diffusion, pp. 121–146. Clarendon Press, Oxford (1956)

[21] Konnik, M.T., Oldham, T., Rzepka, A., Le Maout, V., Stephani, K.A., Panerai, F.: High-temperature oxidation and nitridation of substoichiometric zirconium carbide in isothermal air. Journal of the European Ceramic Society **44**(11), 6771–6776 (2024) https://doi.org/10.1016/j.jeurceramsoc.2024.04.006

[22] Kuriakose, A.K., Margrave, J.L.: The oxidation kinetics of zirconium diboride and zirconium carbide at high temperatures. Journal of The Electrochemical Society **111**(7), 827 (1964) https://doi.org/10.1149/1.2426263

[23] Osei-Agyemang, E., Paul, J.-F., Lucas, R., Foucaud, S., Cristol, S.: Oxidation and equilibrium morphology of zirconium carbide low index surfaces using DFT and atomistic thermodynamic modeling. The Journal of Physical Chemistry C **120**(16), 8759–8771 (2016) https://doi.org/10.1021/acs.jpcc.6b01460

[24] Viñes, F., Sousa, C., Illas, F., Liu, P., Rodriguez, J.A.: Density functional study of the adsorption of atomic oxygen on the (001) surface of early transition-metal carbides. The Journal of Physical Chemistry C **111**(3), 1307–1314 (2007) https://doi.org/10.1021/jp065126i

[25] Rodriguez, J.A., Liu, P., Gomes, J., Nakamura, K., Viñes, F., Sousa, C., Illas, F.: Interaction of oxygen with ZrC(001) and VC(001): Photoemission and first-principles studies. Physical Review B **72**, 075427 (2005) https://doi.org/10.1103/PhysRevB.72.075427

[26] Davey, T., Chen, Y.: The effect of oxygen impurities on the stability and structural properties of vacancy-ordered and -disordered ZrC_x. RSC Advances **12**(5), 3198–3215 (2022) https://doi.org/10.1039/d1ra07768f

[27] Osei-Agyemang, E., Paul, J.-F., Lucas, R., Foucaud, S., Cristol, S., Mamede, A.-S., Nuns, N., Addad, A.: Structure and energetics of ZrC(100)‖c-ZrO_2(001) interface: A combination of experiments, finite temperature molecular dynamics, periodic dft and atomistic thermodynamic modeling. Ceramics International **48**(15), 21327–21343 (2022) https://doi.org/10.1016/j.ceramint.2022.04.099

[28] Osei-Agyemang, E., Paul, J.-F., Lucas, R., Foucaud, S., Cristol, S., Mamede, A.-S., Nuns, N., Addad, A.: Characterizing the ZrC(111)/c-ZrO_2(111) heteroceramic interface: First principles dft and atomistic thermodynamic modeling. Molecules **27**(9), 2954 (2022) https://doi.org/10.3390/molecules27092954

[29] Kwon, S., Rajkamal, A., An, J., Yun, G.J.: Mechanisms of oxycarbide formation on ZrC, HfC, and TaC surfaces during early oxidation: Insights from computational simulations. Ceramics International **51**(11), 14755–14766 (2025) https://doi.org/10.1016/j.ceramint.2025.01.317

[30] Bai, Y., Liang, Y., Bi, J., Cui, B., Lu, Z., Wang, H., You, X., Li, B.: Atomic-scale oxidation mechanism of high-entropy carbides via density functional theory and ab initio molecular dynamics. Journal of the American Ceramic Society **108**(6), 20448 (2025) https://doi.org/10.1111/jace.20448

[31] Newsome, D.A., Sengupta, D., Foroutan, H., Russo, M.F., Duin, A.C.T.: Oxidation of silicon carbide by O_2 and H_2O: A reaxff reactive molecular dynamics study, part i. The Journal of Physical Chemistry C **116**(30), 16111–16121 (2012) https://doi.org/10.1021/jp306391p

[32] Newsome, D.A., Sengupta, D., Duin, A.C.T.: High-temperature oxidation of SiC-based composite: Rate constant calculation from reaxff md simulations, part ii. The Journal of Physical Chemistry C **117**(10), 5014–5027 (2013) https://doi.org/10.1021/jp307680t

[33] Li, H., Jing, Y., Liu, Z., Cong, L., Zhao, J., Sun, Y., Li, W., Yan, J., Yang, J., Li, X.: A machine-learning interatomic potential to study dry/wet oxidation process of silicon. Journal of Applied Physics **136**(9), 095302 (2024) https://doi.org/10.1063/5.0219764

[34] Loew, A., Schmidt, J., Botti, S., Marques, M.A.L.: Universal machine learning potentials under pressure. Journal of Physics: Materials **9**(1), 015010 (2025) https://doi.org/10.1088/2515-7639/ae2ba8

[35] Hong, Q.-J., Walle, A.: Solid-liquid coexistence in small systems: A statistical method to calculate melting temperatures. The Journal of Chemical Physics **139**(9), 094114 (2013) https://doi.org/10.1063/1.4819792

[36] Hong, Q.-J., Walle, A.: Prediction of the material with highest known melting point from ab initio molecular dynamics calculations. Phys. Rev. B **92**, 020104 (2015) https://doi.org/10.1103/PhysRevB.92.020104

[37] Kresse, G., Hafner, J.: Ab initio molecular dynamics for liquid metals. Phys. Rev. B **47**, 558–561 (1993) https://doi.org/10.1103/PhysRevB.47.558

[38] Perdew, J.P., Burke, K., Ernzerhof, M.: Generalized gradient approximation made simple. Phys. Rev. Lett. **77**, 3865–3868 (1996) https://doi.org/10.1103/PhysRevLett.77.3865

[39] Baldereschi, A.: Mean-value point in the brillouin zone. Phys. Rev. B **7**, 5212–5215 (1973) https://doi.org/10.1103/PhysRevB.7.5212

[40] Allen, M.P., Tildesley, D.J.: Introduction. In: Computer Simulation of Liquids, pp. 1–45. Oxford University Press, Oxford (2017). https://doi.org/10.1093/oso/9780198803195.003.0001

[41] Cvitkovich, L., Waldhör, D., El-Sayed, A.-M., Jech, M., Wilhelmer, C., Grasser, T.: Dynamic modeling of Si(100) thermal oxidation: Oxidation mechanisms and realistic amorphous interface generation. Applied Surface Science **610**, 155378 (2023) https://doi.org/10.1016/j.apsusc.2022.155378

[42] Davidson-Pilon, C.: lifelines: survival analysis in python. Journal of Open Source Software **4**(40), 1317 (2019) https://doi.org/10.21105/joss.01317

Supplementary Files

This is a list of supplementary files associated with this preprint. Click to download.

- supplementary.pdf